FDTD Seismic Simulation of Moving Tracked Vehicle

September 2000

Stephen A. Ketcham*, Mark L. Moran*, Roy J. Greenfield[+]

*USACE Engineer Research and Development Center, Cold Regions Research and Engineering Laboratory (ERDC-CRREL), 72 Lyme Rd, Hanover, NH 03755, Stephen.A.Ketcham@erdc.usace.army.mil

[+]Department of Geosciences, Penn State University, University Park, PA 16802, roy@geosc.psu.edu

ABSTRACT

This paper describes the utility of a large finite-difference time domain (FDTD) simulation of seismic wave propagation from a spatially and time varying source that generically represents a moving tracked vehicle. The focus is the computational approach and requirements for the long-duration simulation, the geologic model, the moving vehicle force algorithm, the resulting particle velocity wave fields, and example applications of the data.

The 8th order FDTD simulation consisted of parallel computations based upon a domain decomposition strategy. The computations were performed using a Sun workstation cluster at the U.S. Army Engineer Research and Development Center's Cold Regions Research and Engineering Laboratory (ERDC-CRREL). Our use of such a cluster was necessary because of the spatial extent of the model and the duration of the simulated event; the model dimension is roughly 210 m by 286 m by 80 m (deep) with 1.6-m node spacing, and the event duration is 24.6 s with time steps of 180 μs. The event duration reflects the time required for the vehicle to traverse the model surface at an average speed close to 45 km/h. Three-component particle-velocity wave-field histories over this duration were stored by the simulation for later processing. Models of this extent and duration are on the order of the expected range of coverage for battlefield systems such as Raptor or the Future Combat System sensor system. As a consequence, resulting simulation data can be used for system development in a manner similar to field data.

The moving vehicle forcing history derives from a pressure signal that was measured in near-surface soil beneath a passing armored tracked vehicle. This measurement—a sequence of pressure pulses—was used to empirically design a moving vehicle force algorithm that varies the pulse frequency in proportion to vehicle speed. Spectrograms of surface particle velocities show that this algorithm, together with the FDTD code, produce ground motion responses very much like those measured from field experiments with moving tracked vehicles. These results

Report Documentation Page

Report Date	Report Type	Dates Covered (from... to)
00 Sep 2000	N/A	-

Title and Subtitle FDTD Seismic Simulation of Moving Tracked Vehicle	**Contract Number**
	Grant Number
	Program Element Number
Author(s)	**Project Number**
	Task Number
	Work Unit Number
Performing Organization Name(s) and Address(es) USACE Engineer Research and Development Center Cold Regions Research and Engineering Laboratory (ERDC-CRREL) 72 Lyme Road Hanover, NH 03755	**Performing Organization Report Number**
Sponsoring/Monitoring Agency Name(s) and Address(es) Department of the Army, CECOM RDEC Night Vision & Electronic Sensors Directorate AMSEL-RD-NV-D 10221 Burbeck Road Ft. Belvoir, VA 22060-5806	**Sponsor/Monitor's Acronym(s)**
	Sponsor/Monitor's Report Number(s)

Distribution/Availability Statement
Approved for public release, distribution unlimited

Supplementary Notes
See also ADM201471, Papers from the Meeting of the MSS Specialty Group on Battlefield Acoustic and Seismic Sensing, Magnetic and Electric Field Sensors (2001) Held in Applied Physics Lab, Johns Hopkins Univ, Laurel, MD on 24-26 Oct 2001. Volume 2 (Also includes 1999 and 2000 Meetings), The original document contains color images.

Abstract

Subject Terms

Report Classification unclassified	**Classification of this page** unclassified
Classification of Abstract unclassified	**Limitation of Abstract** UU

Number of Pages
18

reveal the algorithm's adequacy for this stage of our work and guide our concurrent developments to produce source inputs using a sophisticated 3D tracked vehicle mechanical model incorporating suspension dynamics and track-ground interaction.

The geological model consists of two soil layers (above and below a water table) overlying granitic bedrock. Two common geological features distinguish its gently sloping topography: an outcropping of the bedrock and a trench representative of an eroded streambed. Animations of the particle velocity wave fields reveal the vehicle-induced wave propagation and the geology-induced scattering of the waves. These are the first such results produced by seismic models. The application of these wave fields to sensor performance prediction is introduced.

1. INTRODUCTION

The US Army has an interest in the characteristics of seismic surface waves from moving armored vehicles. Using field data Moran and Greenfield (1997) and Prado (1998) have shown that surface waves in mild topographies generally possess high spatial coherence, show smooth amplitude decay as a function of vehicle range, and have little dependence on severe meteorological and seasonal variations. As a consequence these signals are potentially useful to remotely deployed sensor systems that monitor battlefield activities. In support of the Army's seismic sensing needs, we are developing a seismic propagation model that considers the complex effects of topographical features and shallow geological structure on propagating waves. Awareness of these effects can be used to predict system performance and to optimally place sensors.

In this paper we present simulated seismic waves propagating over a topographic surface from a moving tracked vehicle. The vehicle moves across the surface of a geologic model that features a large weathered outcrop of bedrock, two soil layers above the bedrock, and an eroded streambed. Specifically we describe the computation, the geologic model, the representation of the moving vehicle, the resulting particle velocity wave fields, and example applications of the data.

2. COMPUTATIONAL APPROACH AND REQUIREMENTS FOR THE LONG-DURATION SIMULATION

Our requirement to simulate seismic wave propagation in the presence of realistic geologic and topographic features necessitates the use of 3-D numerical modeling. Our method (Moran et al., 1999) follows Hestholm and Ruud (1998), who incorporated surface topography with an appropriate stress-free surface boundary condition into a finite-difference time domain (FDTD) elastic wave propagation model featuring 8th-order, staggered-grid, finite-difference operators. To accommodate surface topography, they express geologic models using a curvilinear grid that is transformed into a rectangular computational grid of equal grid spacing. This mapping can be visualized by proportionally stretching the rectangular grid in the vertical direction so that the free surface matches the topographic function.

Finite-difference seismic simulations over the expected range of coverage for battlefield systems such as Raptor or the Future Combat System sensor system require substantial models and computational durations. In short they are very large computations. As a consequence, our simulation approach consists of parallel computations based upon a domain decomposition strategy (Moran et al., 1999). This requires that the computations be performed on multi-processor computers such as those available at DoD High

Performance Computing Modernization Program (HPCMP) centers. The simulation described in this paper was performed using a 20-processor grid of a multi-processor Sun workstation cluster at the USACE Engineer Research and Development Center's Cold Regions Research and Engineering Laboratory (ERDC-CRREL). The model dimension was roughly 210 m by 286 m by 80 m (deep) with 1.6-m node rectangular-grid spacing. The side and bottom boundaries were set with a 20-cell-thick absorption layer (Cerjan et al., 1985), providing a reduction of at least –25 dB in reflecting wave particle energy. The simulated duration was 24.6 s with time steps of 180 μs. This period reflects the time required for the vehicle to traverse the model surface at an average speed close to 45 km/h. Three-component particle-velocity wave-field histories over this duration were stored by the simulation for later processing.

The simulation ran over nine days on the ERDC-CRREL workstation cluster. The same simulation performed at a DoD HPCMP center could have run in a few hours.

Force inputs to our models must be able to accurately represent the complex mechanical loads generated by tracked vehicles operating over varying topographical surfaces. This objective requires us to focus on the absolute magnitudes of particle velocities resulting from specific force distributions and transients. In previous simulations, by comparison with analytical calculations, we have demonstrated the accuracy of our technique of force input and the resulting propagation in topographic models with highly distorted grid space (Ketcham et al., 2000). We have also demonstrated the accuracy of guided waves in flat-layered models by comparison with wavenumber integration model results and the effects of topography on these waves. We continue with efforts to verify the accuracy of the FDTD simulation technique, which will include further comparisons with independent analyses as well as comparisons with measured field experiment data.

3. GEOLOGIC MODEL

The geologic model is a synthetic model consisting of two fairly stiff soil layers (above and below a water table) overlying granitic bedrock. Two common geological features distinguish its gently sloping topography: an outcropping of the bedrock and a trench representative of an eroded streambed. Figure 1 is a surface contour graph illustrating the topography and these features. Such a setting is typical in glaciated geologic landscapes.

The outcrop is roughly elliptical with dimensions of 80 m by 200 m. Its peak is offset laterally from the center of the streambed by ~150 m. The streambed is roughly 100 m wide by 8 m deep. "Downhill" on the model is from North to South, i.e., from the top of Figure 1 to the bottom, as a gentle 0.002 slope occurs over the model in this direction. The streambed also follows this slope.

Figure 2 illustrates the subsurface layering of the model; it is a slice at the 128-m South-North coordinate. The shades of the model refer to different materials. The upper two layers away from the outcrop are the soil layers. The surface soil layer is approximately 10 m thick. The lower soil layer—i.e., the soil beneath the "water table"—is approximately 15 m thick. The actual values vary throughout the model, as the surface is not smooth. In addition, both soil layers reduce in thickness adjacent to the outcrop due to the increasing elevation of the bedrock surface as it rises toward the outcrop, and the upper soil layer thins toward the streambed.

The outcrop features an upper weathered zone. This zone is depicted in Figure 2 by the shading changes in one-cell-thick layers beneath the outcrop. The uppermost layer in this zone has seismic propagation properties identical to the surface soil layer. The properties vary linearly in six steps until the granitic layer properties are reached. Table 1 lists the seismic propagation properties of the three principal layers.

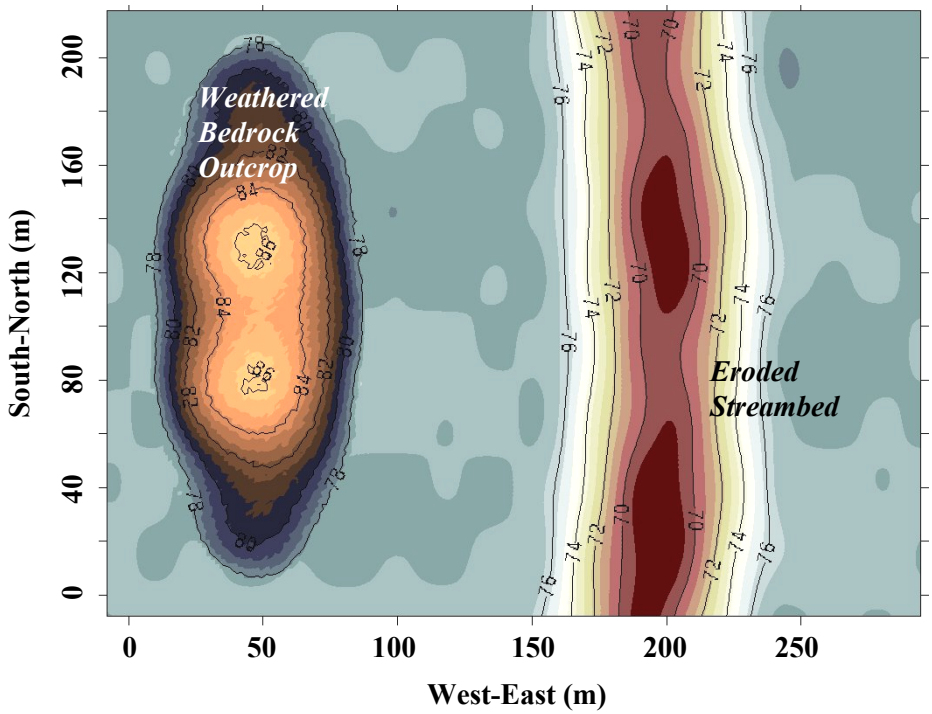

Figure 1. Surface contour graph of geologic model illustrating weathered bedrock outcrop, eroded streambed, and gently sloping flats. Contour values are given in meters above an arbitrary datum.

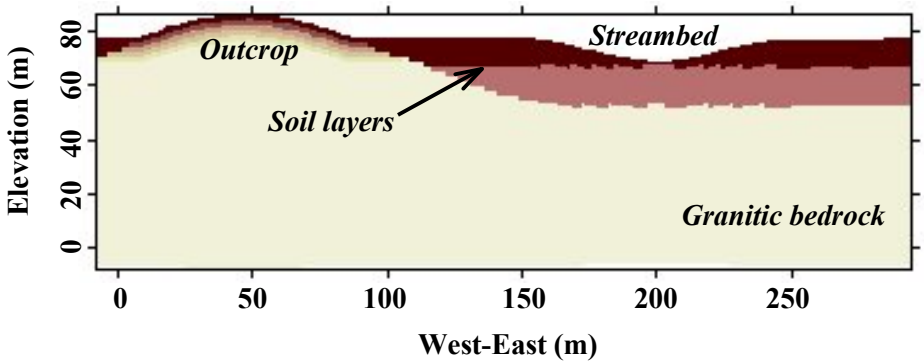

Figure 2. Slice through model at South-North coordinate = 128 m. Distinct shades in graph illustrate layering, with principal layers being granitic bedrock and soil below and above water table. Shading variations in bedrock outcrop are property variations to imposed "weathering."

Table 1. Seismic properties of layer materials in geologic model.

Layer	Compression-wave velocity, V_p, (m/s)	Shear-wave velocity, V_s, (m/s)	Density, ρ, (kg/m^3)
Upper soil layer	1000	577	1750
Lower soil layer	1600	625	2000
Granitic bedrock layer	3500	2333	2650

4. MOVING VEHICLE FORCE ALGORITHM AND LOADING PATH

The forcing history applied in the simulation derives from a force signal that was measured in near-surface soil beneath a passing armored tracked vehicle. This measurement—a sequence of force pulses—was used to empirically design a moving vehicle force algorithm that varies the pulse duration inversely proportional to vehicle speed. Figure 3 illustrates the setup and the idealized result of the measurement. The load cell was located a few centimeters beneath one track of the vehicle while it traversed an unpaved soil layer. The figure depicts a strip-chart-recorder-like trace with wheel-load-generated pulses. The period of the peaks relates to the vehicle speed and wheel spacing as indicated. For this analysis the wheel spacing was set to 1 m, and the maximum force (under the sixth wheel) was set to 100 kN.

The loads were applied as a sequence of vertical point forces over the model surface according to a chosen path and two defined relationships: distance vs. time and speed vs. time. Figure 4 illustrates the path and relationships in parts (a) and (b), respectively. At the appropriate starting time for a given point force in the sequence, the algorithm positions the force on the curved path at the location defined by the path and the total distance traversed. The algorithm finds the nearest finite-difference grid point, and the Figure 3b time series is assigned to load this grid point with a Δt determined by the current vehicle speed.

The empirical force sequence of Figure 3b and its application are precursors to complementary work that is being carried out within the project. Here the emphasis is a moving impulsive load capability. Other details of a rigorous ground loading, such as continuous force equilibrium, are not enforced. The complementary work involves defining the distributed vehicle forces at the track-soil interface in great detail using a high-fidelity mechanical tracked vehicle/suspension dynamics model. Lacombe et al. (2000) present this technique.

5. PARTICLE VELOCITY WAVE FIELDS

Figure 5, parts a-l, depicts images of the vertical particle velocity, w, on the model surface. These images are shown at 2-s intervals over the duration of the simulation, starting at $t = 2$ s. They were constructed from the output of the simulation at each finite-difference grid point on the surface, providing a spatial resolution of 1.6 m. A shaded scale in the figure gives the correspondence between the image shade and the velocity amplitude in m/s. The center of the scale is 0 m/s. Lighter shades indicate positive/upward velocities and darker shades indicate negative/downward velocities. Particle velocity images of this kind provide a physically intuitive picture of the wave propagation; while these images show velocities rather than displacements, the images are not unlike a snapshot of ripples on water caused by a thrown pebble.

Each image was taken from an animation of the particle velocity wave field history that shows the progress of the vehicle along its path by the movement of the concentrated, higher-particle-velocity amplitudes. This animation reveals the continuous vehicle-induced wave propagation and the geology-

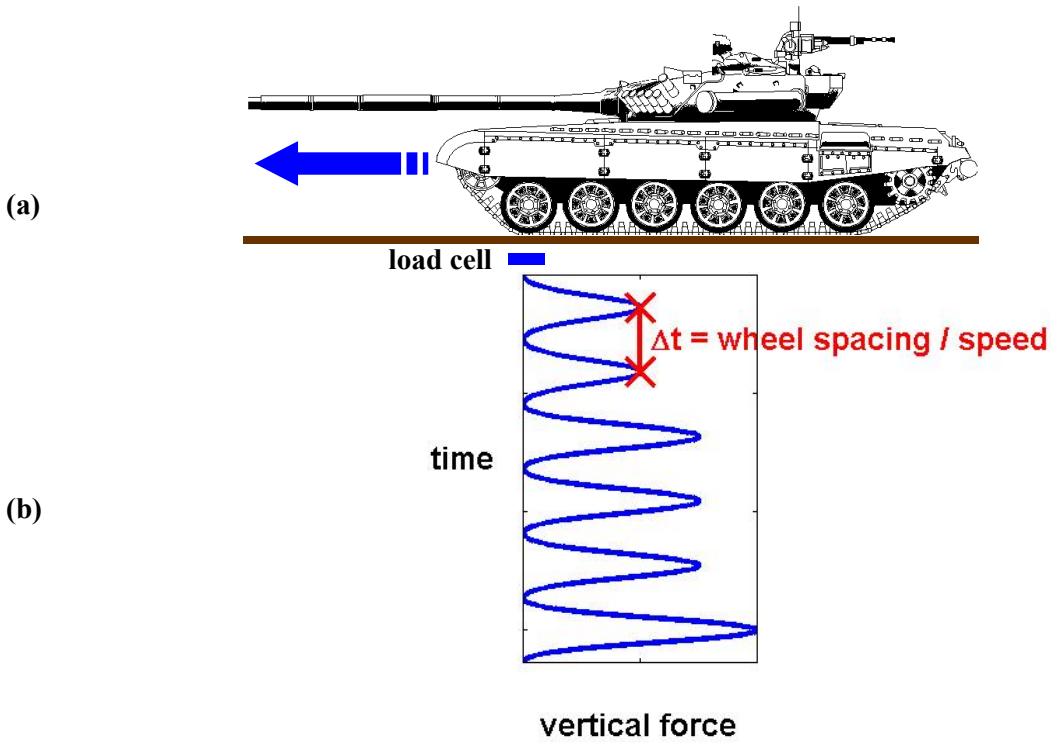

Figure 3. (a) Six-axle tracked vehicle and (b) idealization of force vs. time record from a six-axle tracked vehicle.

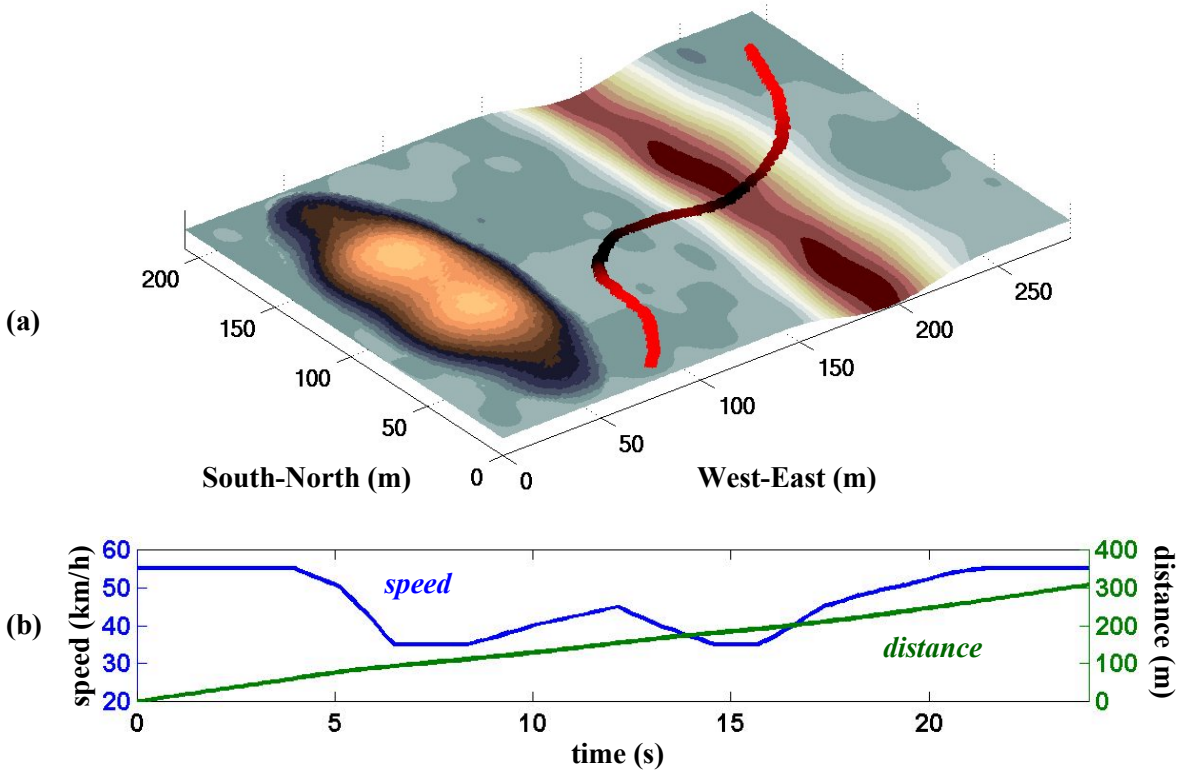

Figure 4. (a) Vehicle path over topographic surface and (b) vehicle speed and distance vs. time.

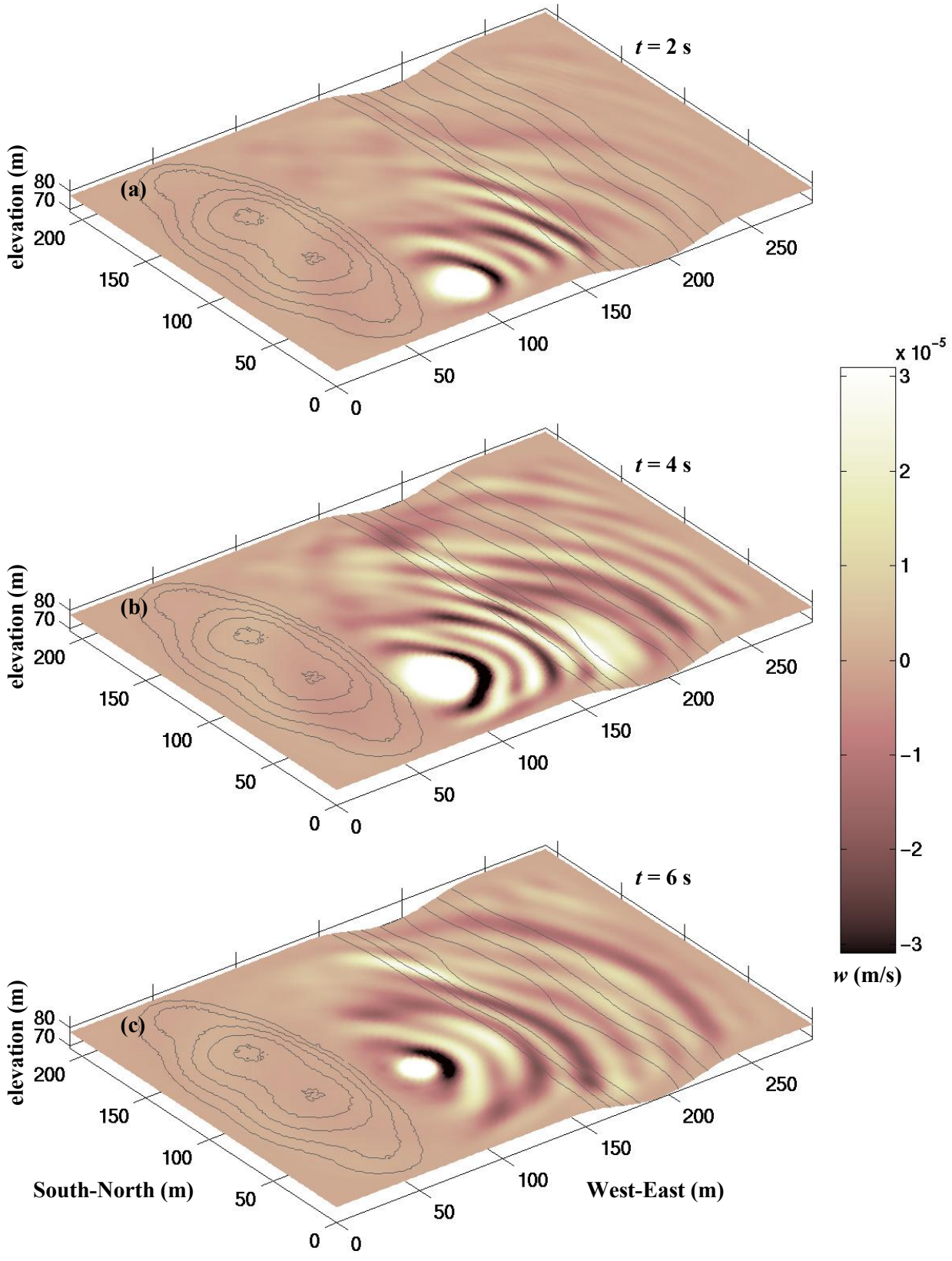

Figure 5. Images of vertical particle velocity *w* on model surface at (a) 2 s, (b) 4 s, and (c) 6 s. Image shade corresponds to value of *w* in colorbar. Contour lines are at 2-m intervals.

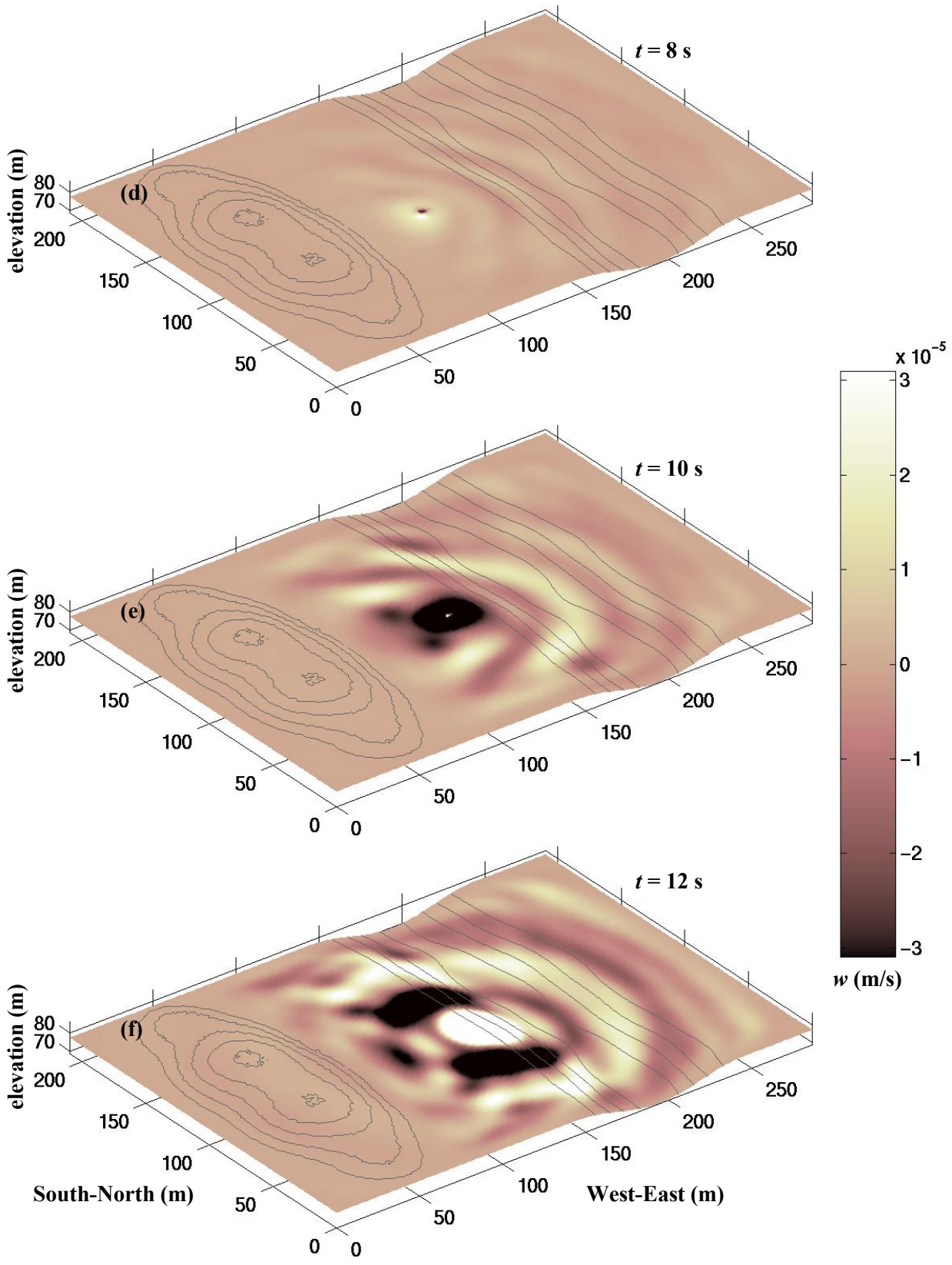

Figure 5 (continued). Images of vertical particle velocity *w* on model surface at (d) 8 s, (e) 10 s, and (f) 12 s. Image shade corresponds to value of *w* in colorbar. Contour lines are at 2-m intervals.

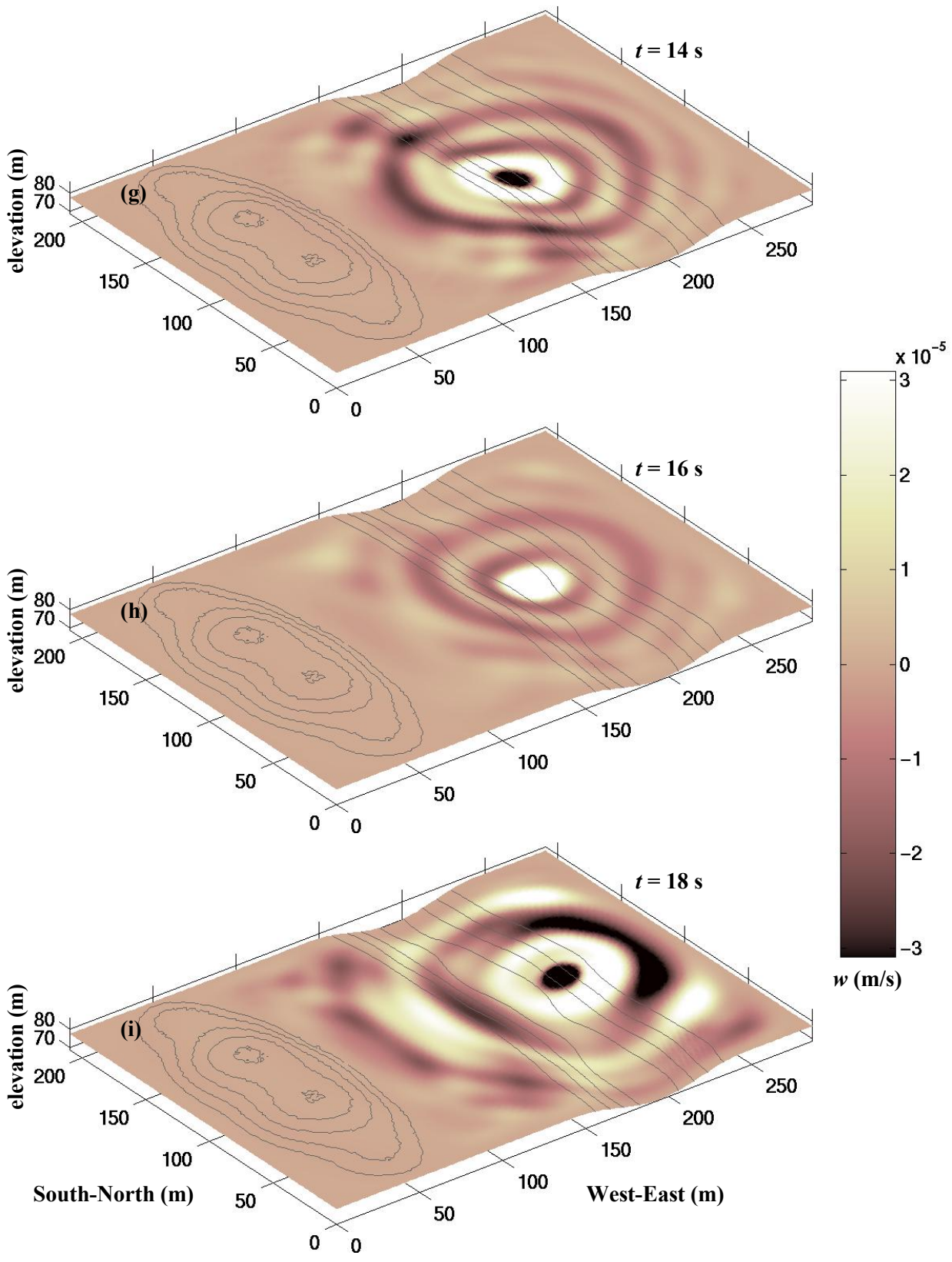

Figure 5 (continued). Images of vertical particle velocity *w* on model surface at (g) 14 s, (h) 16 s, and (i) 18 s. Image shade corresponds to value of *w* in colorbar. Contour lines are at 2-m intervals.

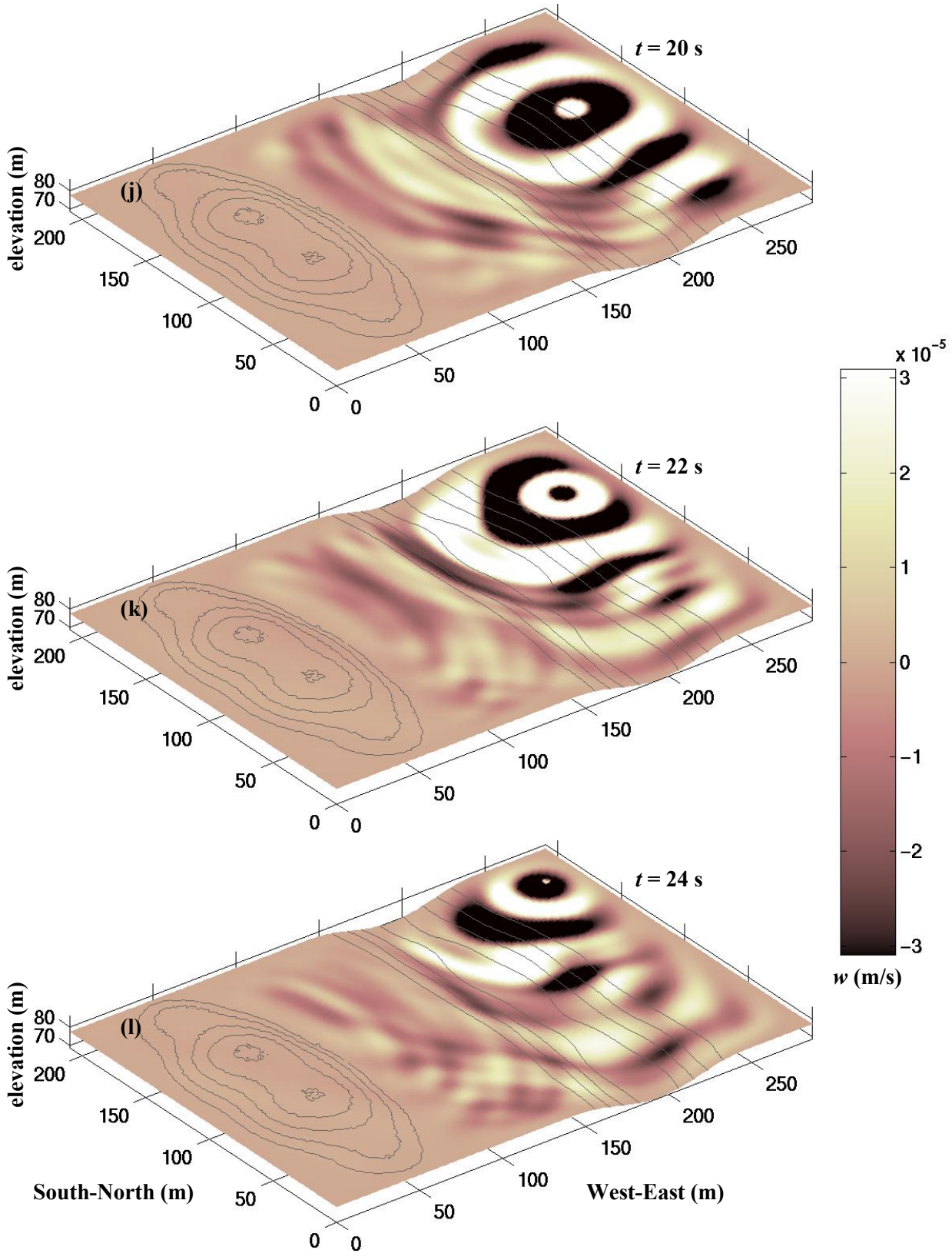

Figure 5 (continued). Images of vertical particle velocity *w* on model surface at (j) 20 s, (k) 22 s, and (l) 24 s. Image shade corresponds to value of *w* in colorbar. Contour lines are at 2-m intervals.

induced diffraction and refraction of the waves. Likewise the still images in Figure 5 reveal features of the propagation. These are discussed here.

The principal waveforms displayed in the images are fundamental Rayleigh surface waves, which have cylindrical decay ($1/R^{0.5}$, R=radius) in the absence of the topography and geology that disturb this decay. The propagation illustrated is that from a continuously moving source, as the forcing time series at a grid point always begins and ends at zero (Figure 3b).

In the initial images of Figure 5a-c, the bending of the wave fronts and the apparent variation in wavelength over the surface shows the effect of the shallow bedrock on the propagation between the outcrop and the trench. As indicated in the geology model slice in Figure 2, this area has soil depths that increase toward the trench. Propagation dominated by bedrock causes the longer apparent wavelengths in the South-to-North direction of Figure 5a-c. Conversely, the lower-velocity soil layers produce the shorter wavelengths seen in the West-to-East propagation.

One possible effect of the streambed on the propagation is the bending of the wave fronts evidenced in Figure 5b. One would expect that the lower, higher-velocity soil layer would impact the propagation direction within the streambed. This appears to be the case, as the wave fronts toward the North end of the trench bend as if they have been accelerated northward by this layer. Figure 5g-k show perhaps clearer indications of this directional bias by the longer wave fronts and faster propagation toward both the South and North directions of the streambed.

A further effect of the trench would be to reflect energy of the surface waves, especially if the bottom of the streambed reached the bedrock (Ketcham et al. 2000). The Figure 5a-c images reveal, however, that this phenomenon does not dominate the propagation as the surface wave energy transmits readily to the lower soil layer and the wave fronts pass the trench with their form intact.

The vehicle speed vs. time graph in Figure 4b indicates that any effect of lower speeds on the propagation should be evident in the period from 6 to 17 s. Indeed, Figure 5d-h from the 8, 10, 12, 14, and 16-s times display longer wavelengths that result from the lower-frequency pulses. Because of the longer wavelengths, however, there is a greater interaction with the deeper, higher-velocity bedrock layer that distorts the wave fronts. The distortion also results in a higher effective surface wave velocity.

In all images of Figure 5 there are much lower particle velocity amplitudes on the rock outcrop relative to the soil layer surfaces. This is because a stiffer, higher-velocity material will vibrate at lower amplitudes in response to the same amount of propagating energy. The stiffness contrast between the rock outcrop and the soil layers causes energy to reflect, moreover, and this is revealed in the reflection patterns between the outcrop and trench in Figures 5f, i, k, and l. Overall the combined effect of the outcrop, trench, and shallow bedrock is to reduce the waveform coherence—i.e., they break up the wave fronts. In general Figure 5 displays obvious and uniform wave fronts in the deeper soil regions and broken or discontinuous wave fronts in locations between the outcrop and ravine. This has considerable impact on vehicle tracking performance, as will be discussed in the next section.

Figure 6 presents vertical particle velocity time series taken from the full wave field results. The signals, shown over the entire simulation duration in Figure 6b, are from the five “receiver” locations depicted in Figure 6a. (West-East, South-North, elevation) coordinates are indicated in Figure 6b. All are on the 106-m South-North coordinate plane. The signals closest to the vehicle path—i.e., the three easternmost receivers—show the strongest response when the vehicle is close to the receiver. In contrast, the two westernmost receivers do not show such a peaky response, as they are farther from the path. The peak level of response in the two western receivers is 1-2 orders of magnitude less than in the eastern receivers, reflecting both the lower amplitude response of the bedrock and outcrop and the remote location of the receivers.

Recognizing (1) that the vertical particle velocity is the quantity that would be recorded in a field measurement by a vertically oriented geophone, and (2) that geophones will be employed in battlefield

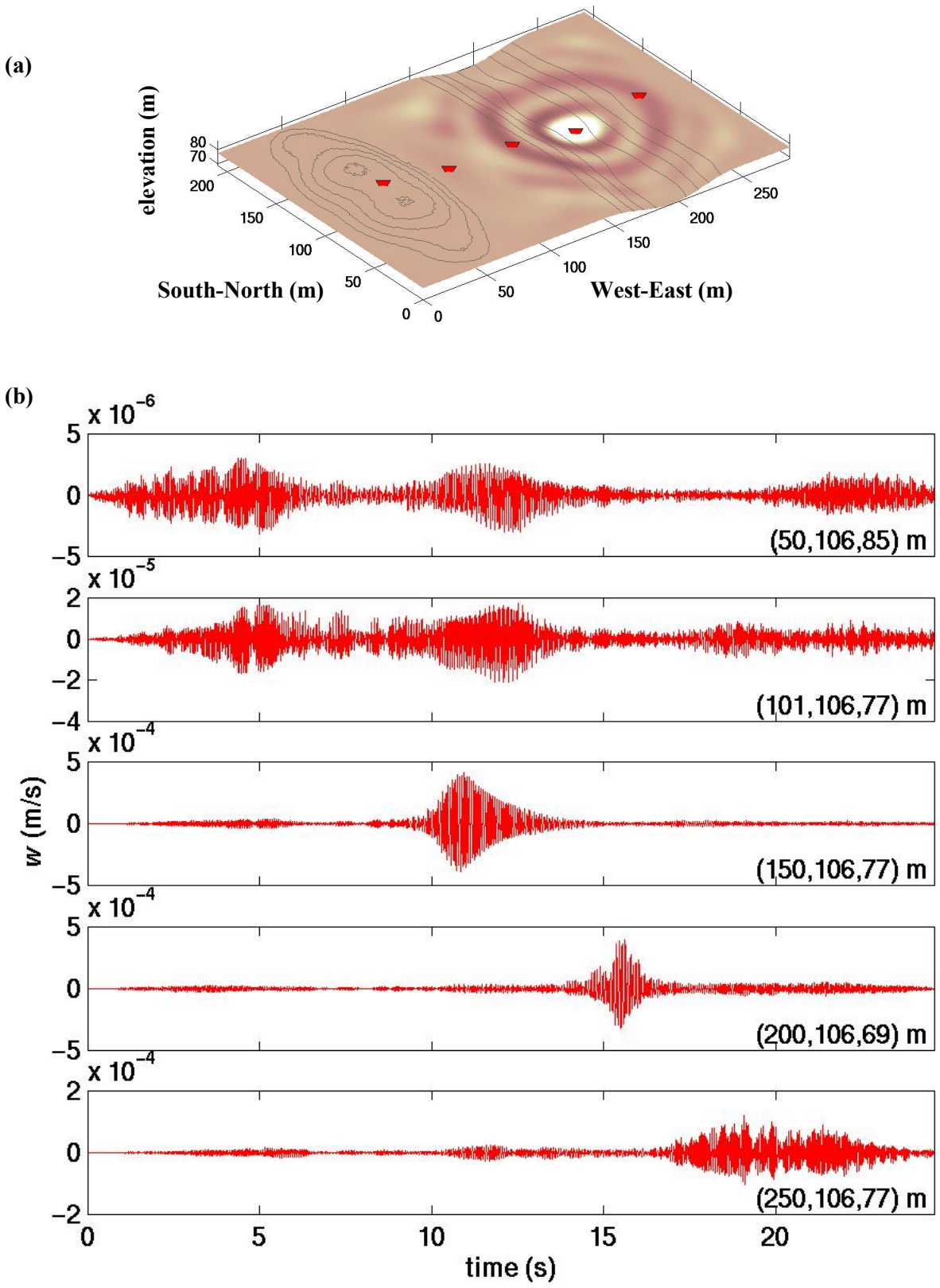

Figure 6. Vertical particle velocity *w* signals at five receiver locations. (a) Receiver locations (shown on *t* = 16-s image), and (b) *w* signals with (S-N, W-E, elevation) location coordinates indicated.

seismic sensors, reveals the utility of simulations like this. Indeed, by providing the full wave field history over the surface of the model, data from simulations can be applied to complement and, in some cases, replace field data in the development and acquisition of systems. Examples of these applications are given in the next section.

6. APPLICATIONS

High-fidelity simulations such as those described in this paper can be used for system development and system performance prediction. Quantitative descriptions of the seismic wave field (Figure 5) over time and space are particularly suited for ground sensor networks since they allow placement of virtual sensors at any point in the simulation domain. Most ground sensor system functions include target detection and system wake-up, target range and bearing estimation, and target classification.

Target classification is generally achieved by estimating spectral features in signals. For seismic signals, Moran et al. (1998b) use spectrograms to display these features. Spectrograms are signal frequency content vs. time images that detail the evolving spectral character of the signal with time (Oppenheim and Schafer, 1989; MathWorks, 1998). They are quantified by calculating successive Fourier magnitudes of a signal using a sliding window and are displayed by plotting each spectrum as a shaded image at the time corresponding to the center of its window.

Figure 7 contains two power spectrograms of the *w* signals from the top-of-outcrop receiver location and the bottom-of-trench receiver location, which were shown in Figure 6. Figure 7 also repeats the speed vs. time graph from Figure 4b for comparison with the spectral variations. The shaded scale in each of Figures 7a and b gives the association between the image shade and the power of *w* relative to 1 $(m/s)^2/Hz$, in decibels. The lighter shades show the frequency content with the highest powers—i.e., the signal spectral content—while the darker shades show the spectral regions with little or no signal power.

The principal signature features of the spectrograms are the multiple harmonic lines at any given time and the clear relationship between the changing spectra and the vehicle speed. These features are very much like those measured from field experiments with moving tracked vehicles (Moran et al., 1998b).

The simulated data can also be used for sensor or system bearing and range performance predictions over regions of the battlespace. For example, Figure 8a gives a map of the wave-field spatial coherence overlain on a contour plot of the terrain topography. Qualitatively, coherence is a frequency domain function between two signals that varies between 0 and 1, with high values indicating a well-defined relationship between the signals. Spatial coherence across an array—i.e., the coherence between one signal in the sensor array and the signals of the other array sensors—provides an indicator of the expected accuracy of array bearing predictions to a seismic source (Moran and Greenfield, 1997), with high and low coherence indicating high and poor performance, respectively. The calculation illustrated in Figure 8a estimated spatial coherence by computing the average coherency at selected points on the finite-difference grid using 25 receiver signals within a 15-m radius of each point. The selected points form a map grid at 15-m spacing in both the South-North and West-East directions. (The 15-m resolution, which was arbitrarily selected and can be improved, is not readily apparent in Figure 8a due to the interpolation used to perform the map shading.) The calculation used a 1-s interval of the wave field data centered at the simulation time 5 s. The value plotted is that for 25 Hz, a frequency in the midst of strong spectral content (Figure 7a and b). Regions where coherence is high, and therefore where bearing tracking would be most accurate, are presented as green. Regions where bearing estimates would be least accurate are shown as red. Intermediate regions are yellow. The regions of lowest spatial coherence are between the outcrop and trench, illustrating again the ability of the outcrop, trench, and shallow bedrock to break up and reflect the wave fronts.

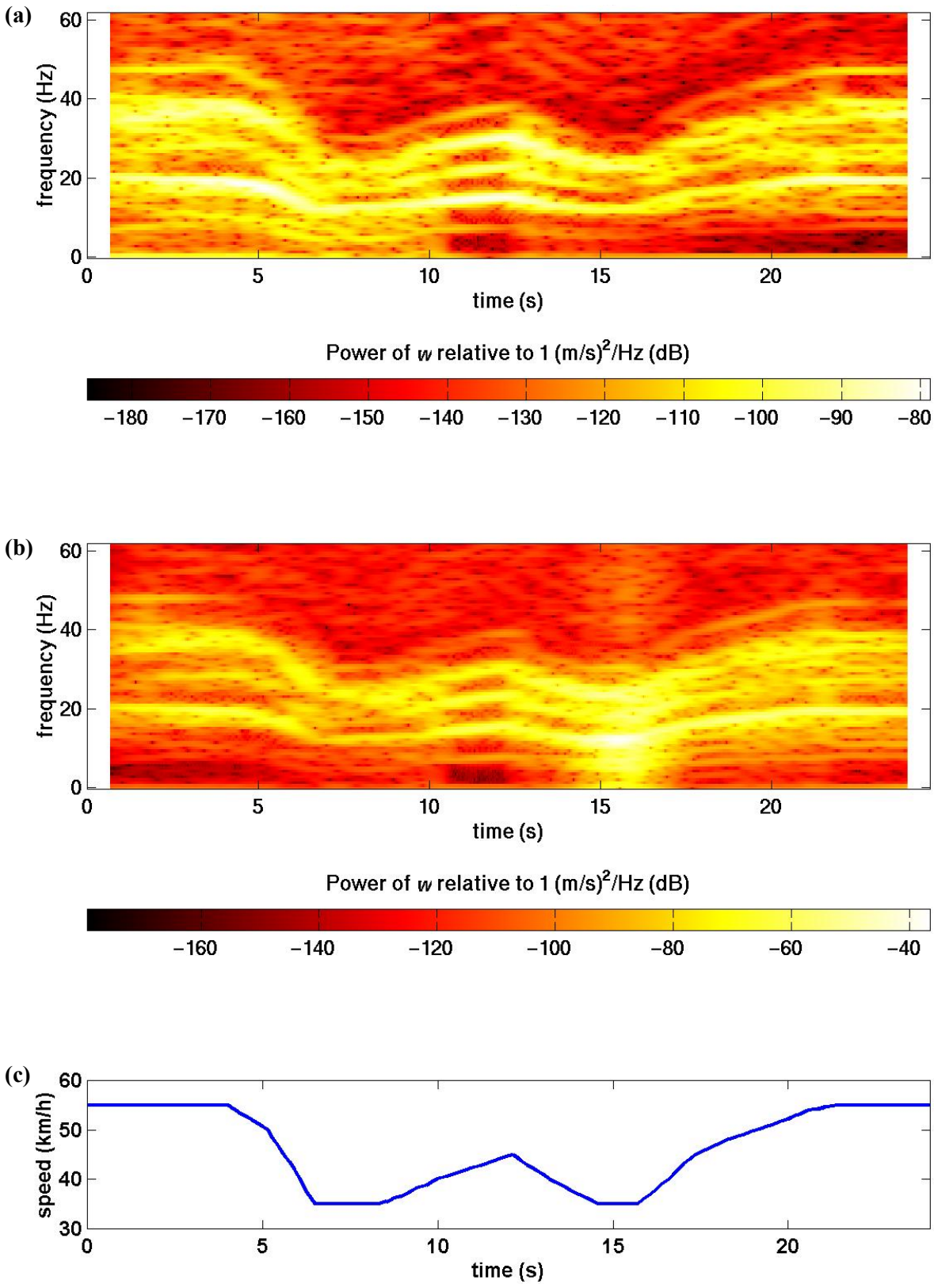

Figure 7. Spectrograms of *w* signals at (a) top-of-outcrop receiver location (50, 106, 85) m and (b) bottom-of-trench receiver location (200, 106, 69) m in comparison to (c) speed vs. time of vehicle.

Complementary to coherence maps are integrated-average amplitude maps. Moran et al. (1998a) demonstrated that knowledge of the spatial variation of wave field amplitude could be used to estimate the range to a moving target. Figure 8b maps amplitude values for the simulated data used in the coherence map. The values are the integrated power spectral density function of the signal at the plotted location. Regions of low amplitude are clearly seen on the rock outcrop, showing the connection to the wave field data in Figure 5. This data can be used for system adaptation thus allowing practical seismic range estimation in battlefield systems.

Simulation-based products also have applications in tactical circumstances. For example, in Figure 9, five seismic tracking arrays are deployed at various locations in the simulation domain. Time series data are extracted from the wave field data at each sensor location within an array, and bearing estimates are formed using methods described by Moran and Greenfield (1997). In Figure 10 the resulting bearings are compared to the true vehicle position. In the case of array 3, the bearing accuracy is very high over the entire duration of the vehicle movement. In the case of array 2, the bearing accuracy is poor due to the low wave field coherence. Firing fans for each array position can be quantitatively defined by stipulating a bearing accuracy requirement. Locations where these firing fans overlap define optimal target engagement zones. This is illustrated conceptually on Figure 9 using the Figure 10 bearing estimates.

7. CONCLUSION

The moving vehicle simulation we have presented is the first such simulation produced by a seismic model. The synthetic wave field particle velocity images reveal realistic and expected seismic propagation physics. Furthermore, the simulated tracked vehicle signatures contain the principal features of seismic vehicle signatures observed in field measurements of moving tracked vehicles. These results clearly show the capability of the simulation model and vehicle force algorithm.

Our example applications demonstrate the utility of the simulations for system development and user situational awareness. Coherence and amplitude maps, when applied to a specific system, can indicate performance in the simulated battlespace. Other quantities such as target bearing can be estimated, and their impact on tactical situations can be tested.

More generally these results provide a strong indication that simulations have a role in seismic system development and acquisition. Their impact can be seen as reducing system costs and development time, improving system performance in complex environments, and allowing propagation physics to be incorporated into system algorithms.

8. REFERENCES

Cerjan, C., Kosloff, R., and Reshef, M., 1985, A Nonreflecting Boundary Condition for Discrete Acoustic-Wave and Elastic-Wave Equations, *Geophysics*, V. 50, pp. 705–708.

Hestholm S., and Ruud, B., 1998, 3-D Finite-Difference Elastic Wave Modeling Including Surface Topography, *Geophysics*, V. 63, pp. 613–622.

Ketcham, S., Moran, M., and Greenfield, R., 2000, The Effect of a Topographic Depression on Guided Seismic Surface Waves, Expanded Abstracts With Biographies, 2000 Technical Program, Volume II, Proceedings of the SEG International Exposition and Seventieth Annual Meeting, Society of Exploration Geophysicists, Tulsa, OK, ST 1.6, pp. 2213-2216.

Lacombe, J., Moran, M., and Happel, S., 2000, A 3-Dimensional Dynamics Model for Generation of Tracked Vehicle Seismic Signals, Prepared for the 2000 Meeting of the MSS Specialty Group on

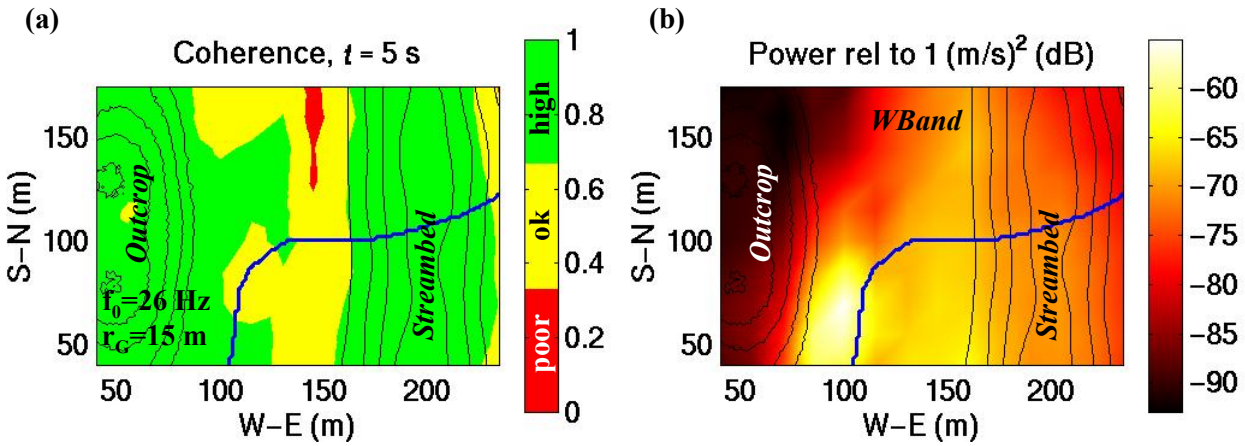

Figure 8. (a) Map of 26-Hz spatial coherence at 5-s simulation time. The map indicates regions where bearing tracking will be most accurate (high) and least accurate (ok-poor). (b) Map of amplitude values for the simulated data used in the coherence map. The values are the integrated power spectral density function of the signal at the plotted location.

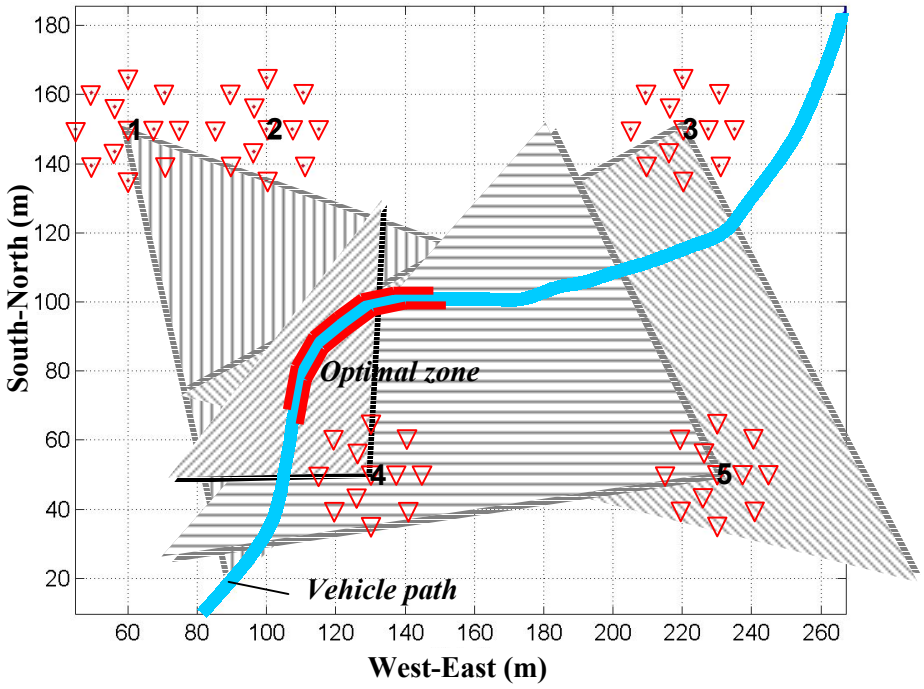

Figure 9. Locations of five virtual sensor arrays using simulated vehicle data. Target bearings can be calculated from the data, resulting in the four "firing fans"illustrated. Each array's firing fan defines an optimal target engagement zone. (Array 2, located in a region with marginal coherence, did not produce a bearing estimate with sufficient accuracy.)

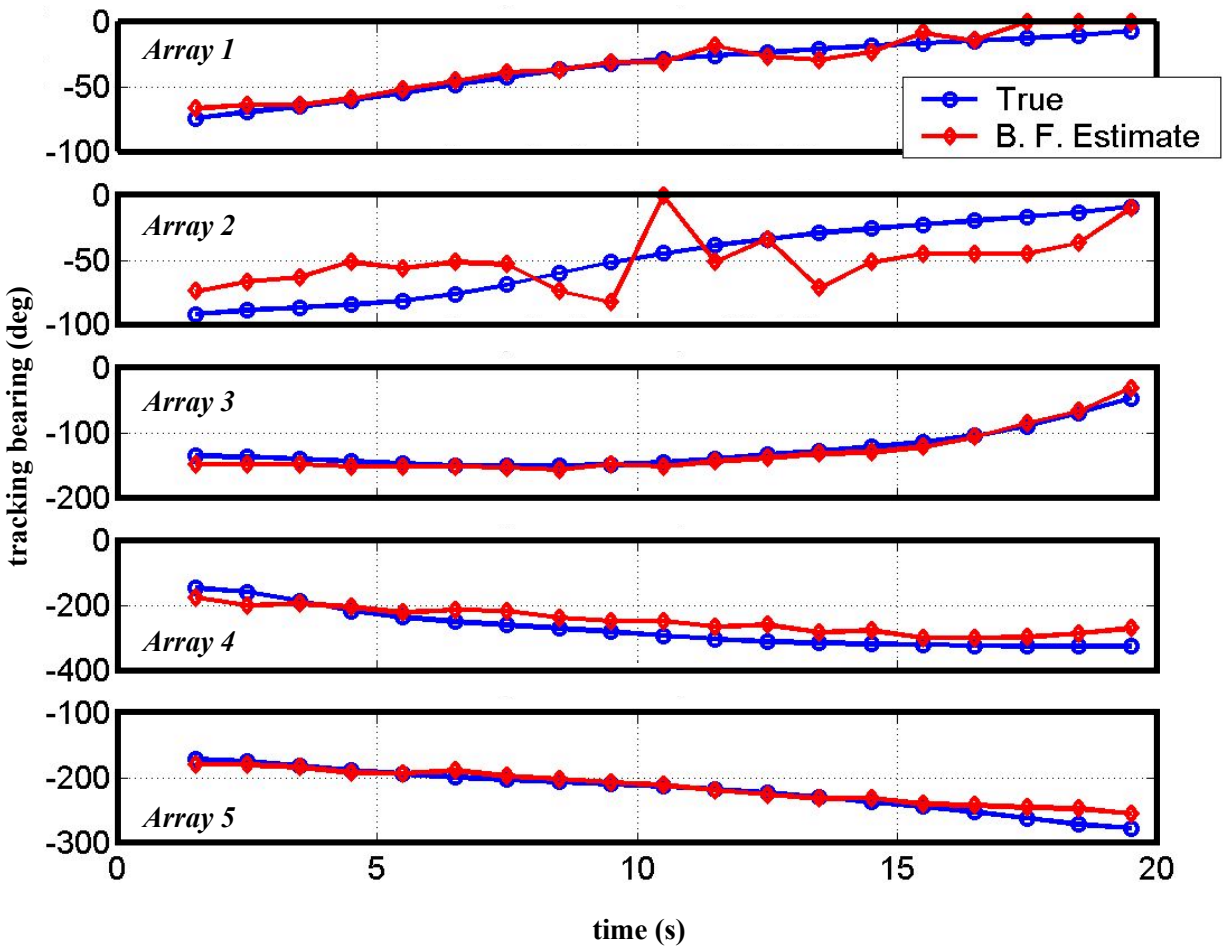

Figure 10. Array bearing estimates (B. F. Estimate) compared with true target bearings (True) from simulated vehicle data. Results are given for arrays 1-5 with locations depicted in Figure 9.

Battlefield Acoustic and Seismic Sensing, 17-19 October, Johns Hopkins University/Applied Physics Laboratory.

MathWorks, Inc., 1998, Signal Processing Toolbox User's Guide, Version 4, The MathWorks, Inc. Natick, MA.

Moran, M., and Greenfield, R., 1997, Seismic Detection of Military Operations, 97-CEP-511-1, U.S. Army Maneuver Support Battle Laboratory, Ft. Leonard Wood, MO.

Moran, M., Boulanger, P., Greenfield, R., Gilligan, T., 1998a, Range Estimation with Seismic Sensors for Early Detection, Final report 98-CEP-0505, Maneuver Support Battle Lab, U.S. Army Engineer School, Ft. Leonard Wood, MO.

Moran, M., Greenfield, R., Prado, G., Turpening, R., Peck, L., Kadtke, J., Carnes, B., Bass, H., Detsch, R., Hawley, B., and Ketcham, S., 1998b, Seismic Feasibility Study in Support of Hornet, Final report of PM-MCD Seismic Eagle Team, U.S. Army ARDEC, AMSTA-DSA-MCD, Picatinny Arsenal, NJ.

Moran, M., Ketcham, S., and Greenfield, R., 1999, Three Dimensional Finite-Difference Seismic Signal Propagation, Proceedings of the 1999 Meeting of the MSS Specialty Group on Battlefield Acoustic and Seismic Sensing, Report 440000-147-X, ERIM International, Inc., Ann Arbor, MI, pp. 1-12.

Oppenheim, A., and Schafer, R., 1989, *Discrete-Time Signal Processing*, Prentice-Hall, Englewood Cliffs, NJ, pp. 713-718.

Prado, G., 1998, Presentation Materials and Personal Communications, Boston, MA, SenTech, Inc.

9. ACKNOWLEDGMENTS

This work was supported by the US Army Office of the Program Manager for Mines, Countermines, and Demolitions under MIPR0KPIC00062. Additional funding was given by the US Army Corps of Engineers, Engineering Research and Development Center, Cold Regions Research and Engineering Laboratory (ERDC-CRREL) under PE62784/AT42. Work at Pennsylvania State University was supported by contract DACA89-99-C-0001 with ERDC-CRREL.